PERGAMON

International Journal of Solids and Structures 38 (2001) 1681–1697

INTERNATIONAL JOURNAL OF SOLIDS and STRUCTURES

www.elsevier.com/locate/ijsolstr

On the development of an osseo-ligamentous finite element model of the human ankle joint

F.A. Bandak *, R.E. Tannous, T. Toridis

School of Engineering and Applied Science, The George Washington University, Department of Mechanical and Aerospace Engineering, Academic Centre, 801 22nd Street, Washington DC 20052, USA

Received 26 July 1999; in revised form 15 December 1999

Abstract

A three-dimensional finite element model of the human ankle joint has been developed to study the mechanisms of impact injury to the major bones of the foot. The model is based on anatomically realistic bone geometry obtained from medical imaging and includes the major ligaments of the ankle. Careful consideration was given to model the soft tissues of the plantar surface of the foot. The model was used to simulate axial impulsive loading applied at the plantar surface of the foot. The stability of the ankle joint was achieved in the model strictly by the intrinsic anatomical geometry and the ligamenteous structure. The time history response of input/output accelerations and forces compared reasonably well with experimental data. Results indicate that the calcaneus experiences the highest stresses followed by the tibia and talus. This is in agreement with several experimental data on calcaneal fracture in axial dynamic loading. Also, the model gives stress localization in the lateral–collateral ligaments that agrees with injury observations for that region. The significance of the model lies in its potential uses as a research tool for understanding the mechanical response of the ankle related to injury and degenerative disease.

Keywords: Impact biomechanics; Finite elements; Orthopaedic

1. Introduction

Lower extremity trauma is common among athletes involved in high-energy sports, and among car crash occupants. According to Thomas et al. (1995), there are more than 100,000 ankle fractures that occur each year in the United States. Full recovery from these injuries is not always possible, resulting in great disruptions in the lives of the victims. They come at a great cost to society due to temporary and permanent impairment and disability (Mackenzie, 1986). It is estimated that the medical cost of ankle fracture repair is around $10,000 on average (Miller et al., 1995). The understanding of the mechanical behaviour of the ankle joint under injurious situations can enhance the delivery of treatment and rehabilitation services. It can also play a major role in the prevention of injury.

* Corresponding author.
E-mail address: fbandak@seas.gwu.edu (F.A. Bandak).

0020-7683/01/$ - see front matter
PII: S0020-7683(00)00129-3

Epidemiological, clinical and biomechanical studies have implicated axial impact to plantar surface of the foot as a main cause of lower extremity trauma (States, 1986; Pattimore et al., 1991; Kallina et al., 1995). Studies conducted by Radin et al. (1973) and Simon et al. (1972) have indicated a relationship between excessive levels of axial loads generated from gait and the damage of the articular cartilage in the lower extremity. Wosk and Voloshin (1981) and Voloshin et al. (1981) studied the capability of the human shock absorber system to attenuate input dynamic loading during gait. Using accelerometers mounted to specified points at the knee, pelvis, and head, the authors determined the percentage of peak acceleration attenuation offered by each body region. They observed a 30% reduction of the peak of the impulses at the knee and 70% attenuation at the head. Voloshin and Wosk (1981) also showed that healthy subjects possess more efficient shock-absorbing capability than do subjects with joint disorders. Recently, Yoganandan et al. (1995, 1996) evaluated the biomechanics of the human-ankle complex under axial impact. The applied dynamic axial loads to the heel of cadaveric specimens and observed fracture. Values of 15.1 kN (SD = 2.7) and 10.2 kN (SD = 1.5) were determined for the mean dynamic forces at the plantar surface of the foot and the proximal end of the tibia, respectively. Both of these values were of sufficient magnitude to cause ankle fracture.

Over the past 20 years, the finite element method (FE) has evolved into a well-established computational tool in biomechanics (Huiskes and Chao, 1981; King, 1984). Once validated, a FE model can be used as a tool for parametric investigation of stress distribution in biological structures. Recently, three-dimensional FE models for investigating the response of lower extremity to dynamic loads have been developed and reported (Beaugonin et al., 1995; Tannous et al., 1996). The rationale for this research is that a FE model of the human lower leg can facilitate the understanding of lower leg injury mechanisms and can be used in a variety of applications in the medical and safety arenas.

2. Methods

2.1. Model geometry

The three-dimensional FE model was created using medical imaging data for the 26 bones of the foot along with the tibia and fibula. PATRAN/P75 (MSC/PATRAN, 1997) was utilized to construct the model. The human bone was constructed by taking into account of the two distinct bone types with different material properties. These are referred to as compact (or cortical) bone and trabecular (or cancellous) bone. Compact bone always surrounds the trabecular bone and its thickness varies from one location to another (Cowin, 1991). A major difference between compact and trabecular bone is the variation in the apparent density. The apparent density of compact bone is 1.8 g/cm^3 (1.68×10^{-4} lb m/in.^{3}), whereas the apparent density of trabecular bone varies between 0.1 g/cm^3 (9.35×10^{-6} lb m/in.^{3}) and 1.0 g/cm^3 (9.35×10^{-5} lb m/in.^{3}) (Cowin, 1991). To represent this important characteristic of the structure, the inner and outer contours of the bones were extracted slice by slice from the imaging data and imported into PATRAN under different groups to allow easy graphical manipulation (Fig. 1a). Fourth order and cubic spline interpolations were used to represent the different tissue boundaries yielding a set of eight smooth and continuous curves (Fig. 1b). This step required assurance of the compatibility (start/end points of curves) between adjacent curves to enhance the quality of the FE mesh. The resulting b-spline curves of adjacent sections were used to define the surfaces giving five surfaces per section with four defining the thickness of the compact bone and one surface defining the surface of the trabecular bone (Fig. 1c). Solids representing the bones were constructed by specifying a series of surfaces from adjacent sections (Fig. 1d) using a technique that ensures slope and curvature continuity. Several solids were generated to describe the different bones of the lower extremity and to include their corresponding compact and trabecular thickness. Proper orientation and relative spacing of the bones was based on radiographic data (Steel et al., 1980).

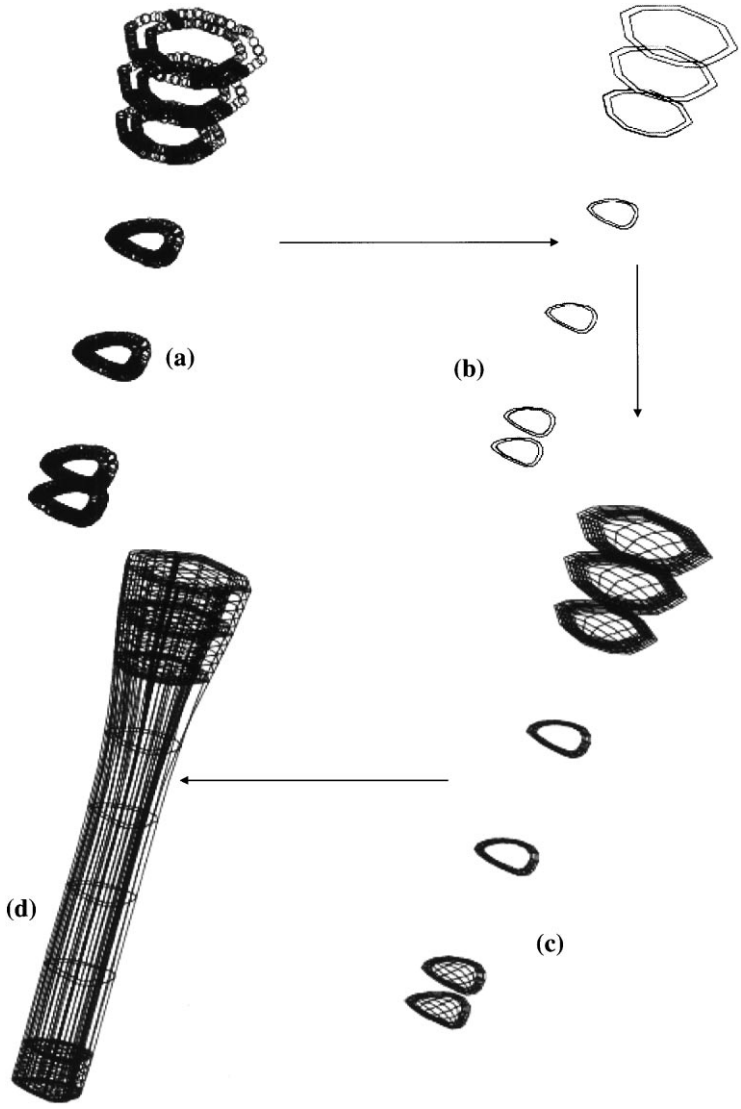

Fig. 1. Sample process of extracting geometry from CT scan data: (a) first, points defining the boundary between compact and trabecular bone are extracted, (b) second, contour lines are produced, (c) third, outer and inner lines are then connected by surfaces, and (d) fourth, the surfaces are converted into solids that describe the whole bone.

The model was then adjusted to include anatomically realistic, matching, articular surfaces between the bones. This was accomplished through a process that involved the following steps. First, proximal and distal bounding surfaces of adjacent bones where the cartilage is located were identified. Second, a copy of the distal bounding surface was produced by applying the manifold surface option in PATRAN. The "manifold option" was used to create a smooth, congruent, spline surface that lies directly on top of the old surface. This is important because the new surface serves as the other part of the contact interfaces between the cartilage and the bone. Third, a parametric solid was generated between the two resulting surfaces. The model was then adjusted to give anatomically realistic matching articular surfaces between the bones, and specifically, those between the calcaneus/talus, the talus/tibia, the talus/navicular, the calcaneus/cuboid, and the fibula/talus.

The ankle ligaments, interosseous membrane, and retinacula were added to the geometry of the model as well as the soft tissues of the plantar surface. The origin, insertion, and average dimensions of the ligaments were obtained from existing data (Anderson, 1983; Williams et al., 1989; Siegler et al., 1988; Parenteau and Viano, 1996). The plantar facia was modelled as three layers each to account for a particular anatomical feature. The first layer simulated the short and long ligament, located directly underneath the bones. The second layer represented the intermediate muscle layer of the flexor digitorium brevis and adductor digiti minimi muscles. The third, is an outer layer representing the plantar aponeurosis, fat, and skin around the sole of the foot.

2.2. Finite element model

The model was developed using a fine mesh, at the surface of contact between the bones, in order to provide a smooth interaction between these surfaces, and a coarser mesh elsewhere. Mesh seeds at the different solid edges were utilized to allow some degree of control over mesh refinement. Eight node linear, isoparametric, brick elements were used. Several verification algorithms were employed within PATRAN to assess the mesh quality. Table 1 presents the different components of the three-dimensional model. The fibula, tibia, calcaneus, talus, interosseous membrane, and the plantar soft tissue were modelled by deformable hexagonal solid elements. The ligaments and retinacula were modelled by deformable membrane elements. The achilles tendon was modelled by a one-dimensional truss element. The remaining foot bones were modelled as rigid bodies. Bone interactions were controlled using contact interfaces and ligament attachments. Thus, slide surfaces were identified between the tibia, talus, fibula, calcaneus, medial and lateral malleoli. The joints between the forefoot and midfoot were not modelled explicitly. Both regions were merged together. This assumption was made because the main focus of this analysis is the impulsive axial loading of the ankle joint. The ankle kinematics, for this case, are determined mainly by talo-crural (talus–tibia–fibula), subtalar (talus–calcaneus), and transverse tarsal (talus–navicular, calcaneus–cuboid) joints (Manter, 1941) and the forefoot plays a minor role, if any, in this case. Additionally, the axial load path is primarily through the heel with little effect on the midfoot and forefoot.

The model contains 21,256 nodes with 16,596 elements out of which 33% were part of the rigid body components. Fig. 2 shows two views of the model. The calculations were conducted using LS-DYNA3D version 940.1, an explicit non-linear large deformation dynamic finite element code.

2.3. Material properties

With the exception of the tibia, little data is available on the mechanical properties of the foot bones. This is also the case for the mechanical properties of the various soft tissues of the arch of the foot, particularly dynamic properties. Bone is generally reported to be a non-homogeneous, viscoelastic material

Table 1
Various components of the three-dimensional model of human ankle

Bones	Ligaments	Retinacula	Tendon/soft tissue
Talus	Deltoid	Flexor retinacula	Achilles
Calcaneus	Anterior talofibular	Superior extensor	Fat pad
Navicular	Posterior talofibular		
Cuboid	Anterior tibiofibular		
Cuneiforms (3)	Posterior tibiofibular		
Metatarsals (5)	Calcaneofibular		
Hallucis (4)	Cervical		
Tibia	Long plantar		
Fibula	Short plantar		

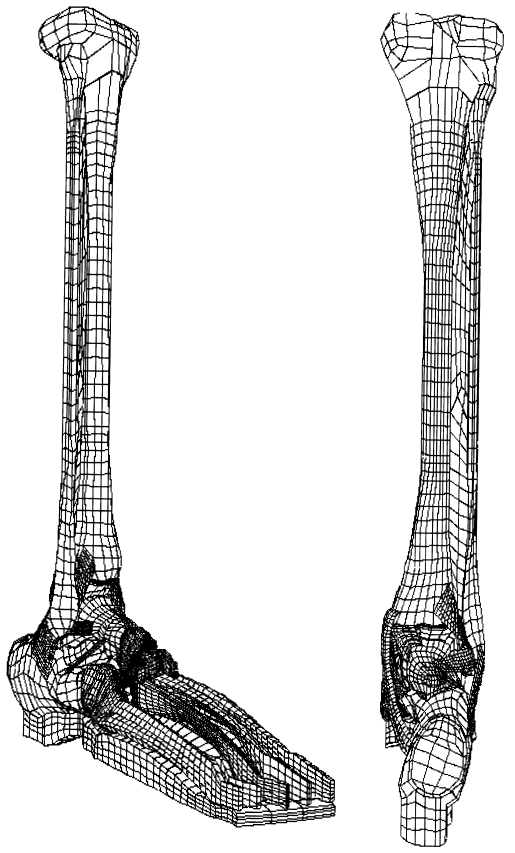

Fig. 2. Isometric and posterior views of the three-dimensional FE model of the human lower extremity.

with anisotropic properties. For this analysis two types of bones, compact and trabecular, were modelled, with the boundary between them estimated from medical imaging data. The compact bone was taken to be homogeneous, isotropic, and linear viscoelastic and was assigned a uniform density value of 1.8 g/cm^3 (1.68×10^{-4} lb m/in.^{3}). The compressive elastic modulus of the tibial compact bone was used as the elastic modulus for all the compact bones of the model. This value was determined by Cowin (1991) to be around 19 GPa (1.76×10^6 psi) and with a Poisson's ratio of 0.3.

Trabecular bone was also taken to be homogeneous, isotropic, and linear viscoelastic. The spatial variation in the density of trabecular bone was not taken into account and a uniform average density of 0.5 g/cm^3 (6.54×10^{-5} lb m/in.^{3}) was assumed. The elastic modulus for this bone was determined from an assumed average apparent density value by a cubic relationship (Carter and Hayes, 1977). The relationship between modulus and density is given by: $E = c\rho^3$, where $c = 4249$ MPa cm^9/g^3. Therefore the elastic modulus was calculated to be 531 MPa (7.70×10^4 psi). The three layers of the arch of the foot were considered to be homogeneous, isotropic, incompressible, and linearly viscoelastic. The muscle was assigned an elastic modulus value of 0.15 MPa (22 psi), and the ligament layer was assigned an elastic modulus of 5 MPa (725 psi). The elastic modulus of the fat layer was assigned a value of 20 MPa (2.9×10^3 psi) (Yamada, 1970; Duck, 1990). The articular cartilage was also taken to be isotropic, homogeneous, and linear viscoelastic with an elastic modulus of 0.7 MPa (120 psi) and a Poisson's ratio of 0.49 (Mow et al., 1989).

The viscoelasticity material model used the stress relaxation function $G(t) = G_l + (G_s - G_l)e^{-t/\tau}$, where G_s is the short-term shear modulus, G_l is the long-term shear modulus, and τ is the relaxation constant. The

Table 2
Summary of the material properties utilized in the model

Hard/soft tissue	Elastic modulus (psi)	Poisson ratio	Density (lb m/in.^{3})	Bulk modulus (psi)	Long-term shear modulus (psi)	Short-term shear modulus (psi)
Compact bone	1.76E + 6	0.30	1.68E−4	1.467E + 06	6.769E + 05	5.077E + 05
Trabecular bone	7.70E + 4	0.30	6.54E−5	6.417E + 04	2.962E + 04	2.221E + 04
Articular cartilage	120	0.49	7.00E−5	2.000E + 03	4.027E + 01	3.020E + 01
Anterior talofibular	2175	0.49	7.00E−5			
Calcaneofibular	1595	0.49	7.00E−5			
Posterior talofibular	2175	0.49	7.00E−5			
Anterior tibiofibular	2400	0.49	7.00E−5			
Posterior tibiofibular	2675	0.49	7.00E−5			
Deltoid	1015	0.49	7.00E−5			
Flexor retinacula	3000	0.49	7.00E−5			
Superior extensor	3000	0.49	7.00E−5			
Plantar ligament	871	0.49	7.00E−5	1.452E + 04	2.923E + 02	2.192E + 02
Muscle layer	22	0.49	7.00E−5	3.667E + 02	7.383E + 00	5.537E + 00
Fat layer	2900	0.49	7.00E−5	4.833E + 04	9.732E + 02	7.299E + 02
Achilles tendon	72,500	0.49	7.00E−5			

corresponding bulk and shear moduli for the above materials were then calculated by using the relationships between the isotropic elastic constants. A value of 10 ms was assigned to τ and the long-term shear modulus was taken as 75% of the value of short-term shear modulus for all the viscoelastic components of the model.

The material constants for the ligaments were extrapolated from force–displacement data from tensile tests on isolated ankle ligaments (Attarian et al., 1985; Siegler et al., 1988; Begeman and Aekbote, 1996). The contact surface friction parameter between the bones was assigned a value of 0.02, similar to that of the hyaline cartilage (Williams et al., 1989). The corresponding material values are shown in Table 2.

2.4. Model evaluation

The specific model evaluation in this study involved the simulation of cadaveric lower extremities under impulsive axial impact. In these experiments, human cadaveric lower legs with the ankle initially in the neutral position, were impacted by a 54 lb (24.5 kg) pendulum at various initial velocities ranging from 7.3 ft/s (2.23 m/s) to 22 ft/s (7.59 m/s) (Yoganandan et al., 1995,1996). Fig. 3 describes the schematic of the mini-sled pendulum apparatus and the specimen set-up. The mini-sled consisted of two long ground stainless steel rails rigidly fixed to a steel frame. A slider sat on top of the steel frame and ball bearings. The slider was used to attach the specimen to the mini-sled apparatus. The proximal end of the specimen was connected to the leading edge of the slider by a potting fixation. The distal end of the specimen (sole of the foot) was loaded axially by the impactor. The impactor consisted of an aluminium loading plate attached to a pendulum. A 1 in. (25 mm) synthetic rubber pad was attached to the loading plate that in turn served as the impacting surface to the foot plantar surface. All specimens were ballasted to 35.2 lb (16 kg). The impact force was collinear with the line of the anterior distal one-third tibia. This was done so that the specimen sustained predominantly axial impact forces. A uniaxial accelerometer and a uniaxial load cell attached at the pendulum recorded the input impact parameters. Another load cell and accelerometer were attached to the proximal potting fixation to record the output force–time and acceleration histories. All data were gathered according to SAE J211b specifications at a sampling rate of 12,500 Hz. At impact velocities below 14.6 ft/s (6.7 m/s) two fractures occurred out of eight runs; three out of four specimens

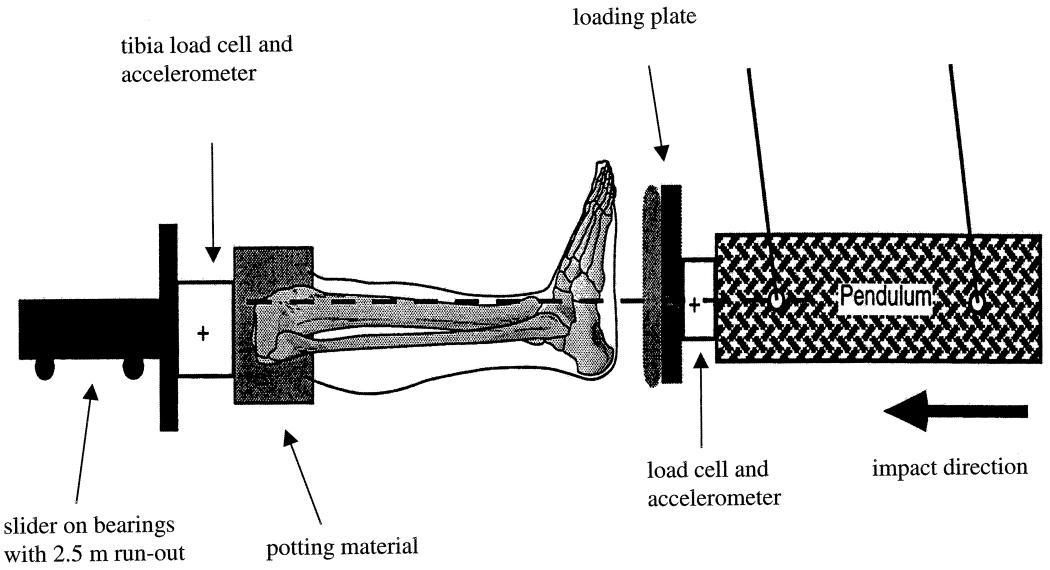

Fig. 3. Illustration of the mini-sled-pendulum set-up along with the knee-foot complex specimen (Yoganandan et al., 1996).

tested at >14.6 ft/s (6.7 m/s) demonstrated intra-articular fractures of the calcaneus and distal tibia with the other remaining intact; and all three specimens impacted at 25 ft/s (7.6 m/s) velocity sustained fractures. The mean impact force to fracture was 2900 lb (13.3 kN). A 54 lb (24.5 kg) rigid plate with a 1 in. rubber impact face was added to the model to simulate the pendulum. The initial position of the plate with respect to the

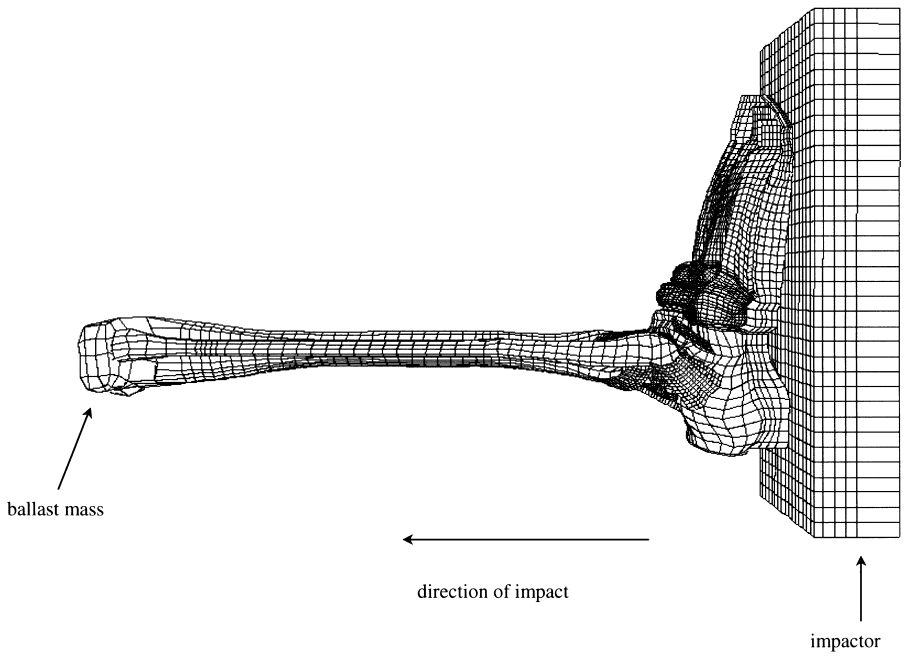

Fig. 4. Simulation set-up.

foot was adjusted to correspond to the experimental set-up. The plate was allowed to move in only one translational direction with all other degrees of freedom fixed. At the distal tibia (tibial plateau) a rigid mass of 25 lb (11.3 kg) was assigned to simulate the weight of the experimental slider. This mass was also constrained to move in the same translational direction as the plate. Several simulations were performed with various pendulum initial velocities of 7.3 ft/s (2.23 m/s), 11 ft/s (3.35 m/s), 14.6 ft/s (4.47 m/s), 17.6 ft/s (5.36 m/s), 22 ft/s (6.7 m/s), and 25 ft/s (7.6 m/s). Fig. 4 illustrates the simulation set-up. The calculations were checked for energy balance for all the impact velocities, and also in all cases, there was virtually no accumulation of hour glass energy.

3. Results

Figs. 5–9 show a comparison of the kinematic response between the numerical simulations and the cadaveric tests. The solid lines indicate the simulation results while the test results are indicated by the

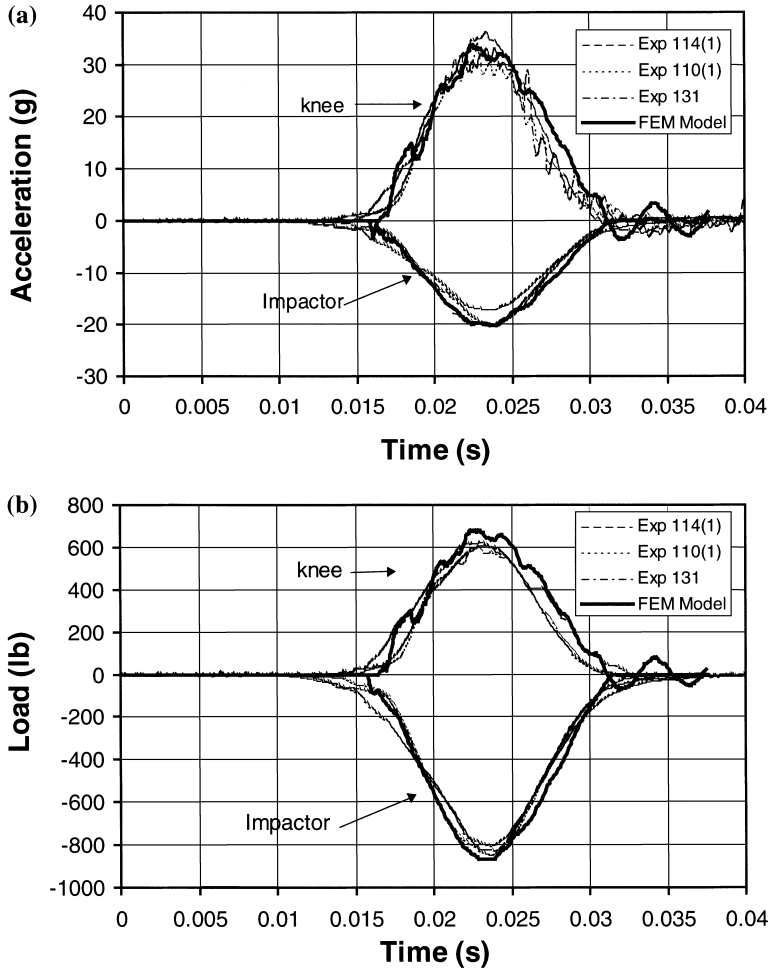

Fig. 5. Comparison of the acceleration and load time histories between FE model and experiments at 7.3 ft/s (2.23 m/s): (a) input parameters and (b) output parameters.

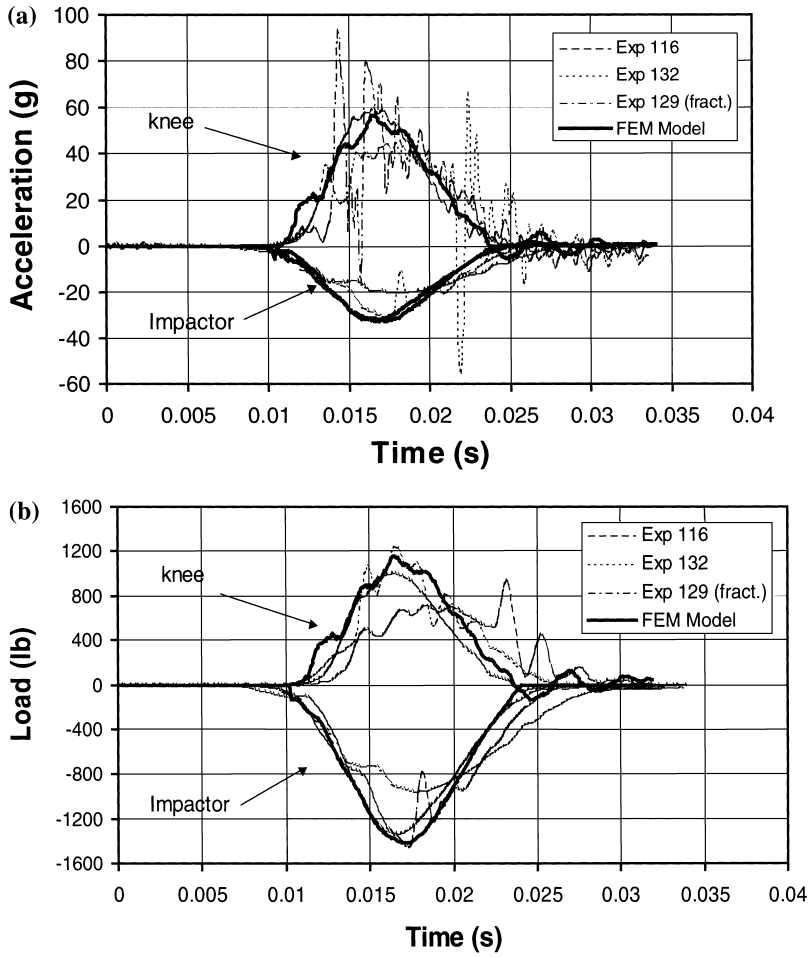

Fig. 6. Comparison of the acceleration and load time histories between FE model and experiments at 11 ft/s (3.35 m/s): (a) input parameters and (b) output parameters.

dotted lines. The shape and pulse duration of input/output acceleration and force time histories between the model and experiments are in good agreement for low impact velocity cases (7.3 and 11 ft/s) with the rise times and slopes being nearly identical. This gives a positive indication that the stiffness and mass distribution of the model are reasonably represented. Table 3 provides a detailed comparison of the input/output kinematic variables between the model and the experiments at various impact velocities. Note that for the same impact velocity, the experimental input force can vary 10–35% and the experimental output force can vary 8–27%. This is expected because of the biological, age, and gender variability of the specimens.

At the higher velocities, for instance the 14.6 ft/s case, the model gives close rise time and pulse duration response compared with the experiments, but the peak amplitude is 28–38% higher for the simulation than experiment (Fig. 7). At 17.6 and 22 ft/s, the difference between the kinematic response from the model compared with the test data becomes pronounced (Figs. 8 and 9). The model gives higher values, although it consistently agrees with the experiments on the rise time of input/output acceleration/force. This gives further reassurance that the model has reasonable inertial and dynamic characteristics.

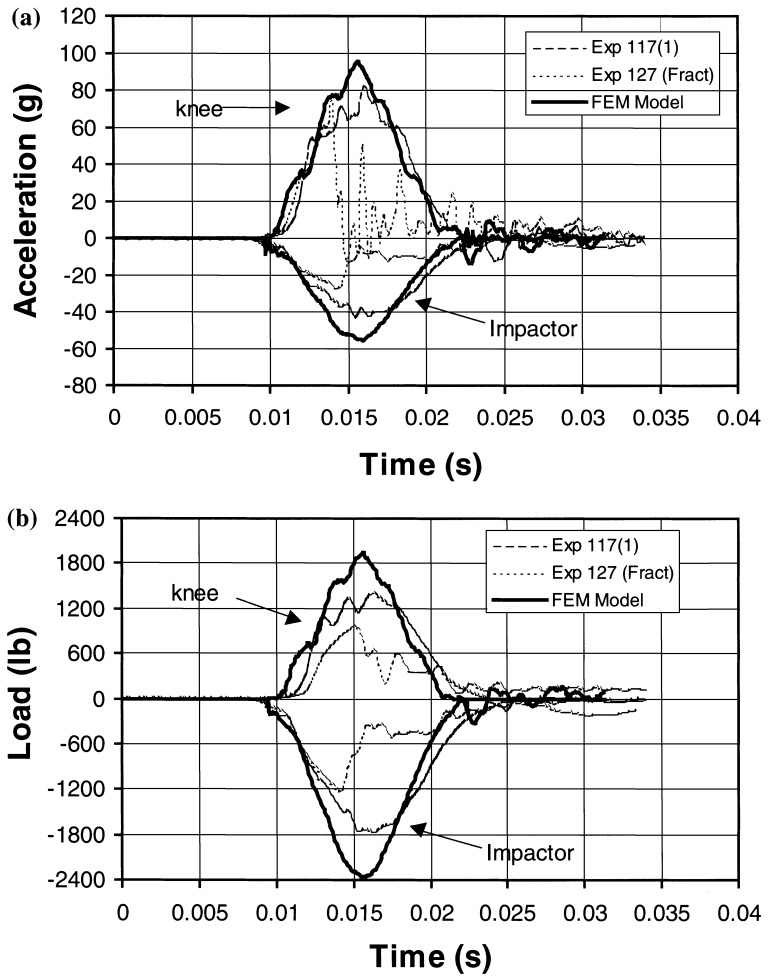

Fig. 7. Comparison of the acceleration and load time histories between FE model and experiments at 14.6 ft/s (4.47 m/s): (a) input parameters and (b) output parameters.

Fig. 10 shows model time history results for the maximum axial compressive stress sustained by the compact bone of the foot for the 22 ft/s case. Two general experimental observations can be confirmed: (1) the calcaneus experiences the highest compressive stresses along the longitudinal axis of the tibia, followed by the talus, tibia, and fibula, (2) peak compression stress values increase as the input accelerations do. These observations were also noted for the Von-Mises, maximum principal stress, maximum principal and strain. Table 4 gives the values for maximum compressive and tensile stresses experienced by the different bones at the 14.6 ft/s impact. It confirms that the calcaneus experiences the highest values. Fig. 11 shows the spatial distribution of the Von-Mises stress viewed posteriorly. It corresponds to the peak input acceleration occurring at about 6 ms. The stress localization in the calcaneus was observed at the inferior surface and near the end of the distal tibia. Fig. 12 shows the Von-Mises stresses for all the ankle ligaments. It shows that the anterior fibulo-talar ligament experiences the highest stresses followed by the deltoid ligament. It indicates that stress localization occurs at the origin and insertion sites for these ligaments consistent with observed injuries in those regions.

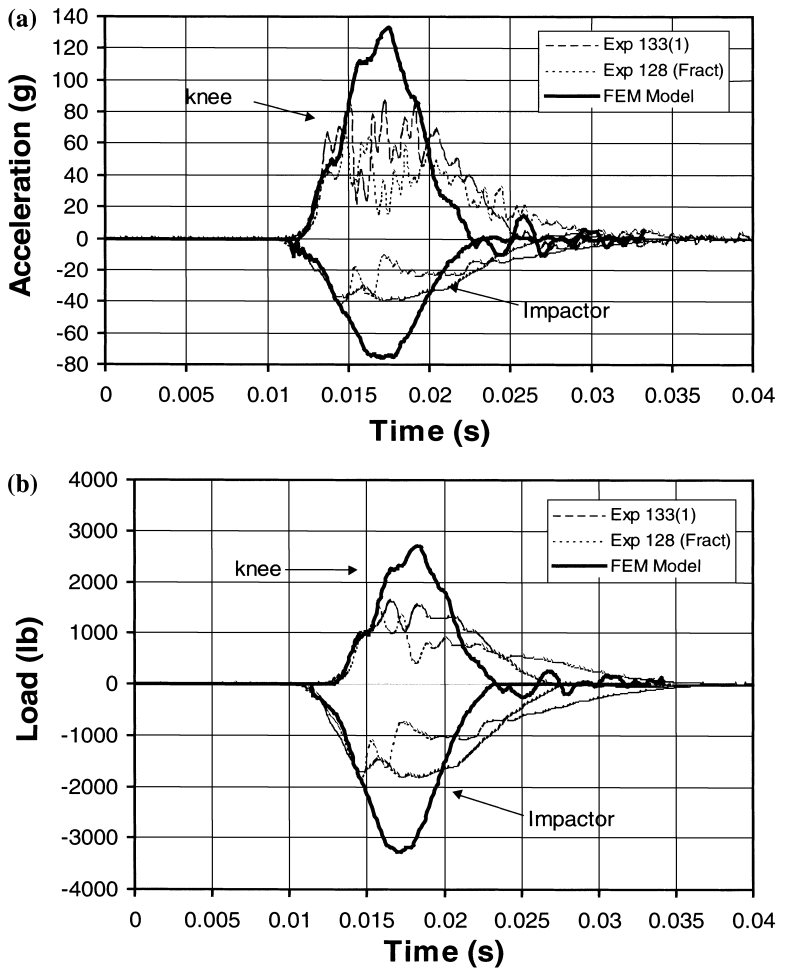

Fig. 8. Comparison of the acceleration and load time histories between FE model and experiments at 17.6 ft/s (5.36 m/s): (a) input parameters and (b) output parameters.

4. Discussion and conclusion

A three-dimensional FE model of the human ankle has been developed and subjected to preliminary verifications against a limited set of experimental data. The model was shown to have reasonable overall mass and stiffness characteristics and is capable of reproducing the experimental input/output responses for a range of impact velocities. At impact velocities greater than 14.6 ft/s (4.47 m/s), however, the model gave higher force and acceleration peak amplitudes than experiment. This discrepancy results from the limited range of applicability of the material models employed and the unavailability of a failure model for bone. The computed model stresses were used as a relative measure of localization since no statistical analysis, accounting for biological variability available. It is possible, however, since the model is based on anatomically realistic geometry that includes various hard and soft tissue components, to take the computed stresses as representative of a possible and realistic loading state in the foot. These stresses compare favourably with published data on bone properties reporting the bone's ultimate compressive strength as

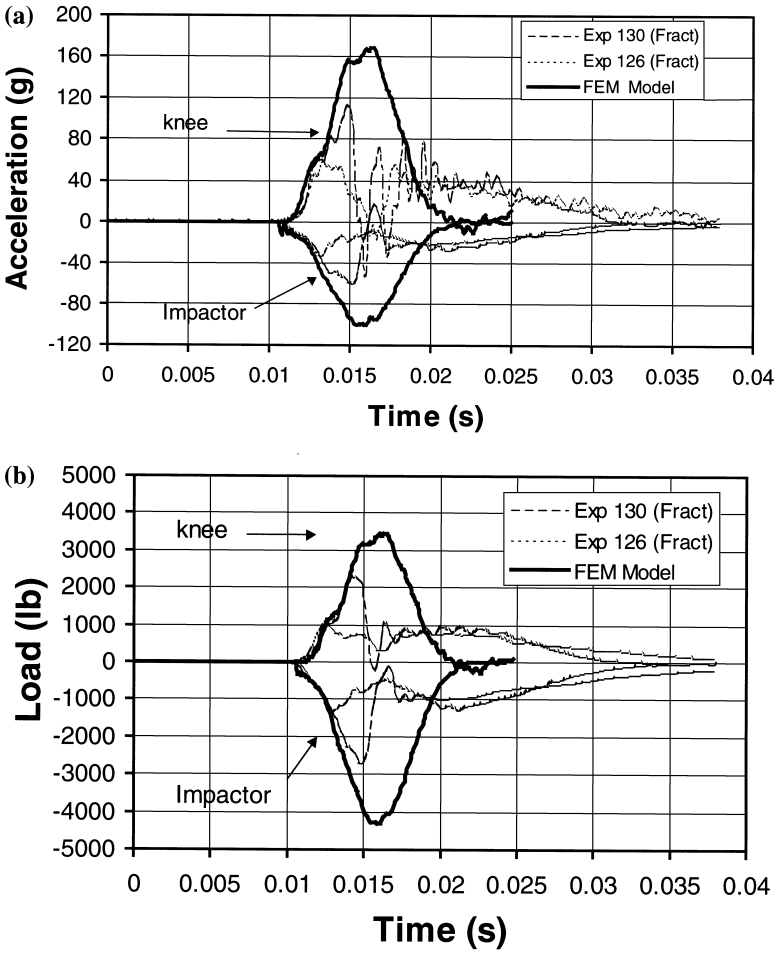

Fig. 9. Comparison of the acceleration and load time histories between FE model and experiments at 22 ft/s (6.7 m/s): (a) input parameters and (b) output parameters.

28,000 psi (195 MPa) (Cowin, 1991). These values were exceeded in the calcaneus for the 14.6 ft/s (4.47 m/s) impact velocity case. The higher stress region is at the inferior level of the bone next to the calcaneal tuberosity that is consistent with experimental observations (Palmer, 1948; Ruedi and Allgower, 1979; Burdeaux, 1983). This phenomenon has also been observed in clinical studies involving injuries from low energy car crashes or falls higher than 2 m (Pattimore et al., 1991; Kallina et al., 1995). The stress localization from the simulations agrees qualitatively with the long crack line observed in most of the specimens that sustained calcaneal fractures (Kitagawa et al., 1998; Yoganandan et al., 1995).

The present model contains several 'advanced' FE modelling features that have not been developed in other reported FE models of the lower extremities (Beaugonin et al., 1995; Schauer et al., 1995). The inclusion of the plantar soft tissue layer of the foot is crucial for adequate simulation of the dynamic response of the ankle (Bennet and Kerr, 1990). The model also provides explicit representation for both compact and trabecular bone. This representation directly affects the mass and stiffness distribution of the individual bones and consequently the model as a whole.

Table 3
Comparison of the input/output force and acceleration between simulation and experiments at: (a) 7.3 ft/s, (b) 11 ft/s, (c) 14.6 ft/s, (d) 17.6 ft/s and (e) 22 ft/s

	Impactor's acceleration (G)	Impactor's load (lb)	Knee acceleration (G)	Knee load (lb)
Simulation	−20.21	−864.00	33.64	−683.00
PCLE114(1)	−20.14	−844.60	35.99	−610.09
PCLE110(1)	−20.14	−824.19	34.17	−601.19
PCLE131	−17.05	−802.40	33.21	−623.54
Simulation	−32.97	−1415.97	56.58	−1157.52
PCLE116	−31.85	−1329.30	59.64	−1002.00
PCLE129 F	−31.70	−1453.00	92.97	−1242.70
PCLE132	−20.21	−953.59	66.85	−936.12
Simulation	−55.14	−2353.80	95.56	−1937.68
PCLE127 F	−27.34	−1222.30	74.68	−970.34
PCLE117	−42.95	−1761.96	82.01	−1402.43
Simulation	−75.72	−3276.99	132.92	−2698.96
PCLE133(1)	−38.94	−1811.90	87.76	−1642.70
PCLE128 F	−41.51	−1833.50	67.73	−1495.5
Simulation	−100.17	−4322.79	168.77	−3448.80
PCLE130 F	−60.43	−2696.80	112.55	−2292.10
PCLE126 F	−32.89	−1334.70	59.75	−1025.70

'F' after a test no. indicates failure.

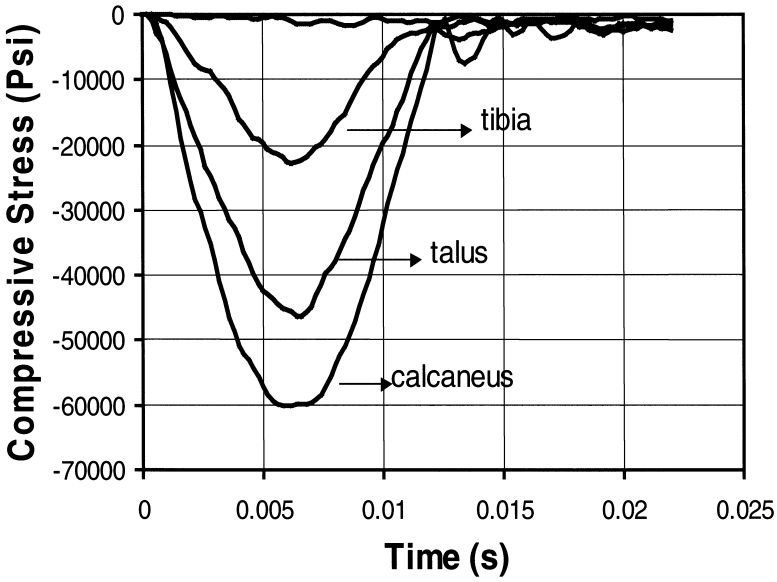

Fig. 10. Time history plot of maximum compressive stress observed in the tibia, talus, calcaneus, and fibula at 22 ft/s (6.7 m/s). The direction of the stress is defined along the tibia's longitudinal axis.

Table 4
Peak values of tensile and compressive stresses experienced by the bones at an impact of 14.6 ft/s (4.47 m/s)

Bone	Maximum tensile stress (psi)	Maximum compressive stress (psi)
Calcaneus	1.73E + 4	2.31E + 4
Talus	1.52E + 4	2.24E + 4
Tibia	1.36E + 4	1.10E + 4
Fibula	7.62E + 3	3.62E + 3

Future work will include testing the model in the variety of kinematic conditions that the model experiences under impact loading. The more generally verified model can then be used in automotive safety and orthopedic applications. More specifically, to aid in providing long-term successful ankle arthroplasty (Stauffer, 1981). The model can help understand some of the main problems associated with ankle prosthetic design such as: (1) over-constraint which causes inadequate stability (Matejczyk et al., 1978) and (2) incongruent contact between the tibial and the talar parts which leads to insufficient support of the normal

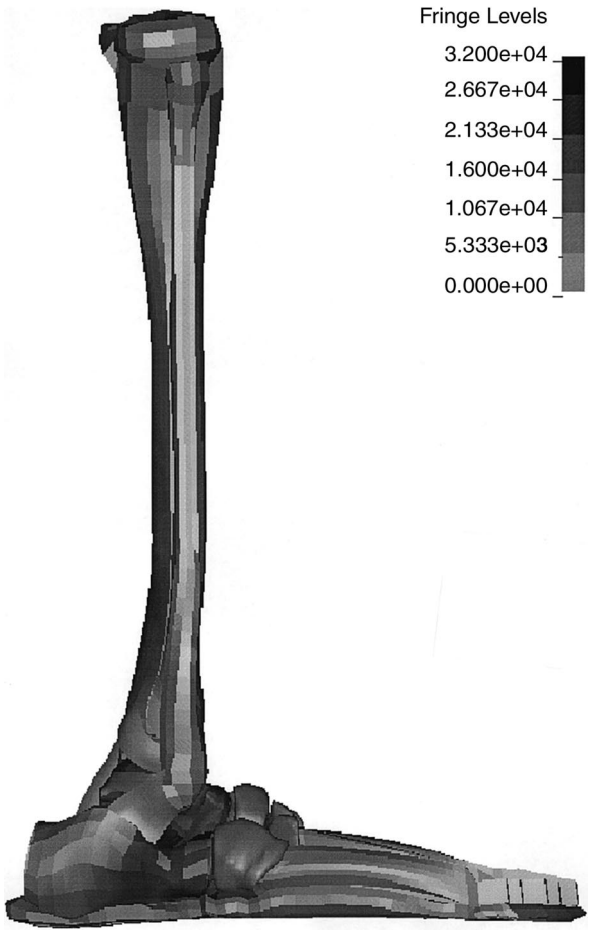

Fig. 11. Spatial distribution of the Von-Mises stresses of the deformable bones for the 17.6 ft/s (5.36 m/s) simulation.

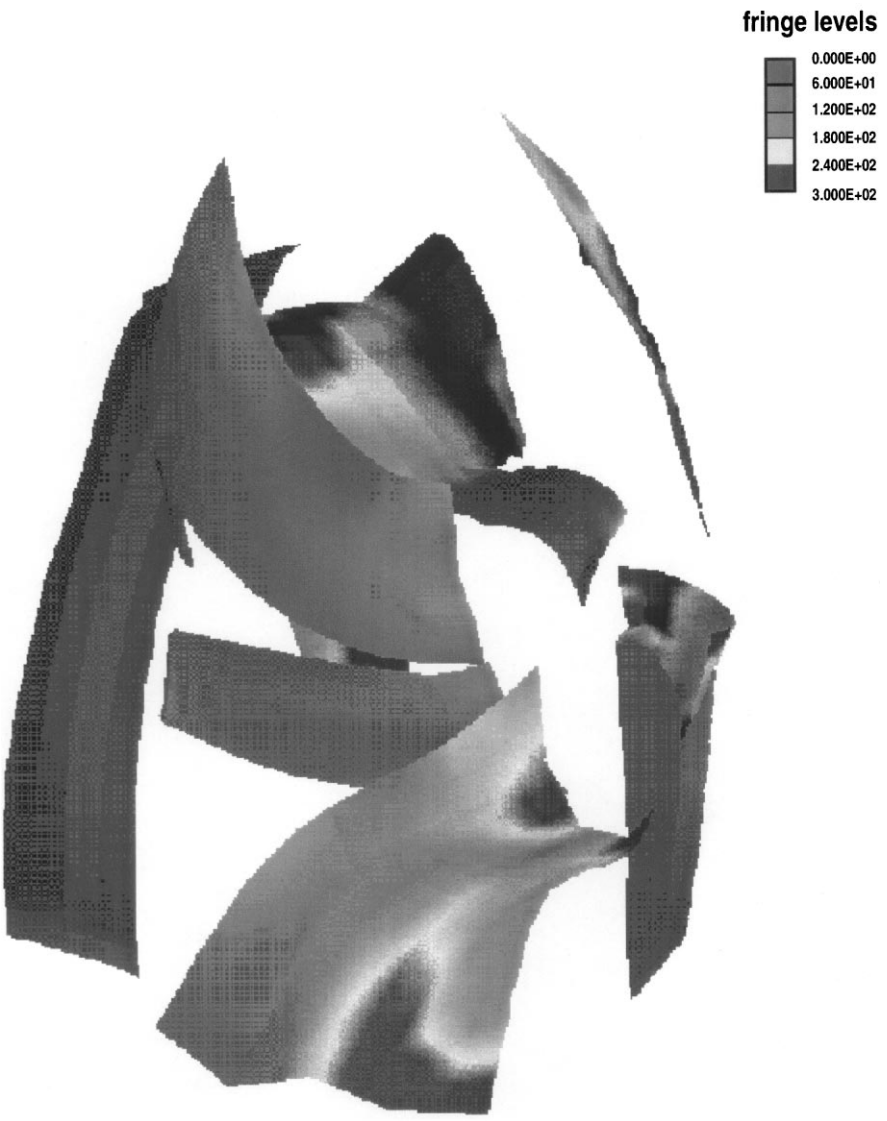

Fig. 12. Spatial distribution of the Von-Mises stresses in the ligaments of the 17.6 ft/s (5.36 m/s) simulation.

ankle loads (Pappas et al., 1976). The model can be further developed to address these difficulties computationally.

References

Anderson, J.E., 1983. Grants's Atlas of Anatomy. Williams & Wilkins, Baltimore MD.

Attarian, D.E., McCrackin, H.J., Devito, D.D., McElhaney, J.H., 1985. Biomechanics characteristics of the human ankle ligaments. Foot and Ankle 6 (2), 54–58.

Beaugonin, M., Haug, E., Munvk, G., Cesari, D., 1995. A preliminary numerical model of the human ankle under impact loading. International Conference on Pelvic and Lower Extremity Injuries Proceedings. pp. 277–289.

Begeman, P., Aekbote, K., 1996. Axial load strength and some ligament properties of the ankle joint. Proceedings of the Injury Prevention through Biomechanics Symposium. pp. 123–135.

Benett, M.B., Kerr, R.F., 1990. The mechanical properties of the human subcalcaneal fat pad in compression. Journal of Anatomy 171, 131–138.

Burdeaux, B.D., 1983. Reduction of calcaneal fractures by the McReynolds medial approach technique and its experimental basis. Clinical Orthopedics 177, 87–103.

Carter, D.R., Hayes, W.C., 1977. The behavior of bone as a two-phase porous structure. Journal of Bone Joint Surgery 59A, 954–962.

Cowin, C.S., 1991. The mechanical properties of cortical bone tissue. In: Cowin, C.S. (Ed.), Bone Mechanics, CRC, Florida.

Duck, F., 1990. Physical Properties of Tissue: A Comprehensive Reference Book. Academic Press, San Diego.

Huiskes, R., Chao, E.Y.S., 1981. A survey of finite element analysis in orthopedics biomechanics: the first decade. Journal of Biomechanics 16, 385–409.

Kallina, I., Scheunert, D., Scheerer, J., Breitner, R., Zeidler, R.B., 1995. Injuries to the lower leg: significance for the occupants-assessment of tests-injury prevention. Proceedings of the Pelvic and Lower Extremity Injury conference. pp. 211–218.

King, A.I., 1984. A review of biomechanical models. Journal of Biomechanical Engineering 106, 97–104.

Kitagawa, Y., Ichikawa, H., King, A.I., Levine, R.S., 1998. A severe ankle and foot injury in frontal crashes and its mechanism. Proceedings of 42nd Stapp Car Crash Conference. pp. 1–12.

Mackenzie, E.J., 1986. Public health impact of lower extremity trauma. Biomechanics and Medical Aspects of Lower Limb Injuries. pp. 161–169.

Manter, J.T., 1941. Movements of the subtalar and transverse tarsal joints. Anatomical Records 80, 397–404.

Matejczyk, M.B., Greenwald, A.S., Black, J.D., Wilde, A.H., 1978. Ankle joint mechanics and implant evaluation. Proceeding of 45th Annual meeting of the American Academy of Orthopedic Surgeons. pp. 34–45.

Miller, T.R., Martin, P.G., Crandall, J.R., 1995. Costs of lower limb injuries in highway crashes. Proceedings of the Pelvic and Lower Extremity Injury conference. pp. 47–57.

Mow, V.C., Proctor, C.S., Kelly, M.A., 1989. Biomechanics of articular cartilage. In: Nordin, M., Frankel, V. (Eds.), Basic Biomechanics of the Musculoskeletal System. Malvern PA, pp. 31–57.

MSC/PATRAN User Manuals, 1997. MSC Engineering, Costa Mesa, California.

Palmer, I., 1948. The mechanism and treatment of fractures of the calcaneus. Journal Bone Joint Surgery 30A, 2–8.

Pappas, M., Buechel, F.F., DePalma, A.F., 1976. Cylindrical total ankle joint replacement: surgical and biomechanical rationale. Clinical Orthopedics 118, 82–92.

Parenteau, C.S., Viano, D.C., 1996. A new method to determine the biomechanical properties of human and dummy joints. Proceeding of International IRCOBI Conference. pp. 183–196.

Pattimore, D., Ward, E., Thomas, P., Bradford, M., 1991. The nature and cause of lower limb injuries in car crashes. Proceeding of the 35th Stapp Car Crash Conference. pp. 47–54.

Radin, E., Parker, H.G., Pugh, J.W., Steinberg, R.S., Paul, I.L., Rose, R.M., 1973. Response of joints to impact loading-III. Journal of Biomechanics 6, 51–57.

Ruedi, T.P., Allgower, M., 1979. The operative treatment of intra-articular fractures of the lower tibia. Clinical Orthopedics 138, 105–110.

Schauer, D.A., Beda, B., Weiss, S., Perfect, S., Moor, E., Kleinberger M., 1995. Lower extremity finite element model development. Proc. of the International Conference on Pelvic and Lower Extremity Injuries, pp. 263–275.

Siegler, S., Block, J., Schneck, C.D., 1988. The mechanical characteristics of the collateral ligament of the human ankle joint. Foot and Ankle 8 (5), 234–242.

Simon, S.R., Radin, E.L., Paul, I.L., 1972. The response of joints to impact loading-II. Journal of Biomechanics 5, 267–273.

States, J.D., 1986. Adult occupant injuries of the lower limb. Biomechanics and Medical Aspects of Lower Limb Injuries. pp. 97–107.

Stauffer, R.N., 1981. Total ankle arthroplasty: four years' experience. Clinical Orthopedics 160, 217–221.

Steel, M.W., Johnson, K.A., DeWitz, M.A., Ilstrup, M.S., 1980. Radiographic measurements of the normal adult foot. Foot and Ankle 1 (3), 151–153.

Tannous, R.E., Bandak, F.A., Toridis, T.G., Eppinger, R.H., 1996. A three-dimensional finite element model of the human ankle: development and preliminary application to axial impulsive loading. Proceeding of the 40th Stapp Car Crash Conference.

Thomas, P.T., Bradford, M., Charles, J., Fay, P., 1995. Lower extremity injuries and their causation in car crashes: real-world accident data collection. Proceeding of the Pelvic and Lower Extremity Injury conference. pp. 15–24.

Voloshin, A., Wosk, J., Brull, M., 1981. Force wave transmission through the human locomotor system. Journal of Biomechanical Engineering 103, 48–50.

Voloshin, A., Wosk, J., 1981. Influence of artificial shock absorbers on human gait. Clinical Orthopaedics and Related Research 160, 52–56.

Williams, P., Warwick, R., Dynson, M., Bannister, L., 1989. Gray's Anatomy atlas. Churchill Livingston.

Wosk, J., Voloshin, A., 1981. Wave attenuation in skeleton of young healthy persons. Journal of Biomechanics 14, 261–267.

Yamada, H., 1970. In: Evans, F.G. (Ed.), Strength of biological materials. The Williams & Wilkins, Baltimore MD.

Yoganandan, N., Pintar, F.A., Boyton, M., Sances, J.A., 1995. Biomechanics of foot and ankle fractures. Proceeding of the International Conference on Pelvic and Lower Extremity Injuries. pp. 201–209.

Yoganandan, N., Pintar, F.A., Boyton, M., Begeman, P., Prasad, P., 1996. Dynamic axial tolerance of the human foot-ankle complex. Proceeding of 40th Stapp Car Crash Conference. pp. 207–218.